Nature Communications

https://doi.org/10.1038/s41467-026-74749-8

Article in Press

Direct imaging-based gradient metasurface sensor enabling spectrometer-free ultrasensitive biomolecule detection

Received: 12 August 2025

Accepted: 15 June 2026

Cite this article as: Kim, H., Yun, H., Jeong, S. *et al.* Direct imaging-based gradient metasurface sensor enabling spectrometer-free ultrasensitive biomolecule detection. *Nat Commun* (2026). https://doi.org/10.1038/s41467-026-74749-8

Hongyoon Kim, Heechang Yun, Sebin Jeong, Min Ryu, Jaehyuck Jang, Chunghwan Jung, Younghwan Yang, Eunji Lee, Minsu Jeong, Yong-Sang Ryu, Hyomin Lee & Junsuk Rho

Direct imaging-based gradient metasurface sensor enabling spectrometer-free ultrasensitive biomolecule detection

Hongyoon Kim[1,#], Heechang Yun[2,3,#], Sebin Jeong[2,#], Min Ryu[2], Jaehyuck Jang[2], Chunghwan Jung[2,4], Younghwan Yang[1,5,6], Eunji Lee[2], Minsu Jeong[1,4], Yong-Sang Ryu[7] , Hyomin Lee[2], Junsuk Rho[1,2,3,8,9,10,*]

[1]Department of Mechanical Engineering, Pohang University of Science and Technology (POSTECH), Pohang 37673, Republic of Korea

[2]Department of Chemical Engineering, Pohang University of Science and Technology (POSTECH), Pohang 37673, Republic of Korea

[3]Quantum Information Science Program, Graduate School of Convergence Science and Technology, Pohang University of Science and Technology (POSTECH), Pohang 37673, Republic of Korea

[4]Polymer Research Institute, Pohang University of Science and Technology (POSTECH), Pohang 37673, Republic of Korea

[5]Department of Mechanical Engineering, Changwon National University, Changwon 51140, Republic of Korea

[6]Department of Smart Manufacturing Engineering, Changwon National University, Changwon 51140, Republic of Korea

[7]School of Biomedical Engineering, Korea University, Seoul 02841, Republic of Korea

[8]Department of Electrical Engineering, Pohang University of Science and Technology (POSTECH), Pohang 37673, Republic of Korea

[9]POSCO-POSTECH-RIST Convergence Research Center for Flat Optics and Metaphotonics, Pohang 37673, Republic of Korea

[10]National Institute of Nanomaterials Technology (NINT), Pohang 37673, Republic of Korea

[*]Corresponding author. E-mail: jsrho@postech.ac.kr

#These authors contributed equally

Abstract

Biosensors play a crucial role in modern diagnostics, where simple, portable systems can enable rapid on-site testing. Here, we introduce a direct imaging-based biosensor capable of reconstructing spectral shifts from transmission images without the need for a spectrometer. By introducing a continuous geometry gradient in a dielectric metasurface, we spatially encode distinct resonance wavelengths across the device, enabling quasi-continuous spectral readout from a single camera image. Our platform achieves a high-quality factor and fine 0.1 nm spectral step size across a broad 30 nm spectral window within a 300 μm footprint, without spectroscopic instrumentation. This direct imaging-based approach exhibits high sensitivity with a figure of merit of 67.2 per refractive index unit and enables label-free detection of both proteins and DNA, reaching a limit of detection down to 388 picomolar. This spectrometer-free biosensor presents a compact sensing platform with a clear pathway toward a potentially more cost-effective implementation than conventional optical refractometric sensors, enabled by a simplified optical architecture facilitating molecular testing beyond specialized laboratory settings.

Introduction

Rapid and sensitive detection is essential for timely clinical decision-making and effective disease management. Point-of-care (POC) diagnostics have gained growing attention as healthcare systems shifts from treatment-centered models to diagnosis-driven approaches. Unlike conventional laboratory-based assays, POC biosensors enable on-site analysis, reducing diagnostic delays and enabling immediate clinical interventions. Such systems are particularly valuable in decentralized or personalized settings, where early detection can trigger prompt treatment and potentially prevent widespread health crises. Optical biosensors that leverage resonant nanostructures have emerged as a powerful approach for POC diagnostics by enabling precise engineering of the interaction between resonant modes and target analytes, offering high sensitivity and label-free detection through spectral response monitoring[1–4]. This allows accurate monitoring of biochemical interactions through optical response, where near-field enhancement and the resonance quality factor (Q-factor) are critical parameters for sensing performance[5].

Plasmonic nanostructures, such as nanoparticles and nanoantennas, have been extensively explored as biosensors due to their strong near-field confinement[6–9]. These structures support surface plasmon polaritons (SPPs) or localized surface plasmons (LSPs), confining electromagnetic fields to subwavelength volumes near metal-dielectric interfaces, enabling high sensitivity to refractive index changes near the surface[10–14]. However, intrinsic ohmic losses in metals fundamentally limit the Q-factors of plasmonic resonances, which in turn restricts the spectral resolution of plasmonic sensors.

Dielectric metasurfaces have recently emerged as a powerful alternative due to their low-loss, non-absorbing material properties[15–19]. Built from transparent high-index materials that exhibit negligible optical absorption in the visible and near-infrared, dielectric metasurfaces support high-Q resonances by minimizing dissipative losses. In particular, the concept of bound states in the continuum (BIC) has enabled extremely high-Q modes in dielectric nanostructures[20–22]. BICs arise from symmetry-protected or interference-induced conditions that confine optical modes without radiation loss. Although an ideal BIC is non-radiative and thus not directly observable, introducing a slight asymmetry converts it into a quasi-BIC that radiates to free space, yielding a tunable Q-factor and strong localized fields[23]. This ability to enable extremely sharp spectral features,

combined with strong near-field enhancement, makes BIC-based dielectric metasurfaces highly suitable for biosensing applications[24–28].

Despite these advances, optical biosensors based on refractometric sensing, which detect spectral shifts caused by local refractive index changes upon target analyte binding, continue to face fundamental limitations. These systems typically rely on bulky high-resolution spectrometer and broadband light sources to accurately readout resonance wavelength shifts. This requirement adds cost and complexity and hinders application for compact POC devices. The challenge is exacerbated for high-Q resonances, which demand fine spectral resolution to detect minute wavelength shifts, making it difficult to implement simple and portable systems. To address this, recent strategies have employed single-wavelength illumination and imaging detection, eliminating the need for a spectrometer[29]. In such an approach, the light source is fixed at a single wavelength near the resonance, and an image sensor monitors intensity changes as the resonance shifts with analyte binding. While this method leverages high-Q resonances for enhanced sensitivity, the inherently narrow linewidth of a high-Q mode means that only small spectral shifts can be detected before the resonance moves out of the fixed illumination band. In other words, increasing the Q-factor improves the sensitivity but simultaneously narrows the spectral window over which spectral shifts can be monitored. Pixelated metasurface have been explored in refractometric sensing to extend the detectable range by incorporating metasurface pixels, each tuned to a different resonance wavelength[21,30]. However, such designs typically support only a limited number of discrete resonances, up to 16 resonances under ideal fabrication, resulting in limited spectral resolution that only partially substitute high spectral resolution spectrometers. Furthermore, they rely on fabrication imperfections to introduce geometric variability within a single pixel to increase the spectral resolution, which ultimately degrades the overall sensor performance.

Here, we introduce an imaging-based gradient metasurface sensor that achieves high Q-factor, fine spectral resolution, and a broad spectral coverage under single-wavelength illumination, all in a compact, spectrometer-free platform (Fig. 1a). The metasurface consists of an array of dielectric nanostructures supporting quasi-BIC resonances, with the unit cell geometry continuously varied along one in-plane axis (perpendicular to the incident polarization). This spatial gradient in unit cell geometry effectively “encodes” a different resonance wavelength into each unit cell of the

metasurface (Fig. 1b). Under monochromatic illumination from a VCSEL laser diode (λ = 760 nm), the device generates a sharp dark line in the transmission image at the position where the illumination wavelength matches the local resonance. When the local refractive index changes, (e.g., biomolecular binding) the resonance wavelength shifts, causing the dark line to move laterally across the image. This spatial displacement effectively translates the small spectral shift into a position change detectable by an image sensor (Fig. 1c). By mapping positions on the metasurface to known resonance wavelengths, the spatial intensity profile in the captured image is translated into a transmission spectrum, allowing quantitative readout of resonance shifts without a spectrometer (Fig. 1d).

We demonstrate the capabilities of this platform through two representative biosensing assays. First, we perform a model protein-ligand detection using biotin-functionalized surfaces to capture streptavidin, a well-known high-affinity pair, to validate specific protein detection at the monolayer level. Second, we functionalize the metasurface with single-stranded DNA probes and detect complementary DNA targets, highlighting the sensor's ability to perform sequence-specific nucleic acid detection. The gradient metasurface demonstrates ultrasensitive detection down to the hundreds of picomolar range, and the imaging-based readout enables these measurements with simple hardware. By eliminating bulky spectrometers and leveraging a monochromatic VCSEL diode for illumination, the platform retains high sensitivity, spectral resolution, and a broad operating range, while offering a compact and practical solution for point-of-care diagnostics.

Results

Design of resonance gradient metasurface sensor

Our gradient metasurface sensor is based on a dielectric nanostructure designed to support high-Q quasi-BIC resonances. We selected customized hydrogenated amorphous silicon (a-Si:H) as the metasurface material due to its high refractive index and negligible extinction coefficient across the region of interest (λ = 600-800 nm) (Supplementary Note 1). The metasurface comprises periodic unit cells patterned in a 100 nm thick a-Si:H film on a glass substrate. Each unit cell contains a pair of elliptical nano-holes etched through the film (Fig. 2a). A hole-type geometry was employed to improve fabrication robustness, particularly to facilitate the formation of a vertical

sidewalls during the reactive ion etching step. The baseline unit cell was defined by a period (P) of 340 nm, an elliptical hole long-axis (W) of 240 nm, short-axis (L) of 144 nm, and film thickness (H) of 100 nm. The elliptical holes are rotated by an angle α with respect to the periodic lattice, introducing an in-plane asymmetry. This asymmetry enables a quasi-BIC resonance. When α is zero, the structure maintains perfect symmetry, resulting in a true BIC with theoretically infinite Q. A nonzero α breaks the symmetry slightly, allowing the mode to couple to free space, yielding a finite Q (Fig. 2b). By varying α, we observed that the resonance Q-factor increases as α decreases (Fig. 2c). We selected $\alpha = 20°$ to balance between high Q-factor and tolerance to fabrication imperfections (Supplementary Note 2). Transmission dispersions were calculated using our in-house rigorous coupled-wave analysis (RCWA) (Fig. 2d), and experimental measurements on the fabricated structures showed strong agreement with the simulated result (see detailed experimental setup for transmission dispersion in Supplementary Note 3). Note that this measurement was performed on metasurfaces with uniform scaling factor across the entire area.

To systematically tune the resonance wavelength across the device, our gradient metasurface was fabricated with a size of 300 × 300 μm^2, where the scaling factor (S) of the unit cells gradually increased from 0.97 to 1.03 along the horizontal axis. This gradient introduces slight variations in both the size and vertical position of the elliptical holes along each unit-cell column, resulting in a continuous modulation of the resonance wavelength from $\lambda = 745$ nm to 775 nm (Fig. 2e). The corresponding spatial resonance map was obtained by sweeping the illumination wavelength from 745 to 775 nm in 0.1 nm increment and identifying, for each pixel, the wavelength at which the transmission reaches its minimum. Importantly, the scaling is applied gradually along the horizontal axis of the metasurface, perpendicular to the incident polarization, to effectively decouple with distinct collective dipole modes (Supplementary Note 4). We experimentally confirmed the spatial gradient in resonance by measuring the transmission spectrum at different horizontal positions on the device, observing a progressive red shift in resonance from left to right (Supplementary Note 5). Scanning electron microscopy (SEM) images taken from the leftmost and rightmost regions of the device (Fig. 2f) clearly show the slight increase in ellipse size between $S = 0.97$ and $S = 1.03$, as well as a subtle vertical shift in the hole pair's position within the unit cell, consistent with the applied scaling (Supplementary Note 6). These structural variations underpin the gradient metasurface's fine spectral resolution and broad spectral coverage.

Under *x*-polarized single-wavelength illumination, the metasurface's quasi-BIC resonance manifests as a sharp dark line in the direct transmission image, corresponding to the set of positions that are resonant at that illumination wavelength (See detailed experiment setup in Supplementary Note 7). In other words, when illuminated with a monochromatic beam, only those unit cells that resonance matches the illumination wavelength will significantly suppress transmission (appearing dark), and because resonance wavelength varies with horizontal position, the dark feature appears along a narrow vertical stripe at a specific horizontal location. As the illumination wavelength increases, the dark line shifts laterally to the right, following the spatial distribution of resonance frequencies (Fig. 2g). We note that near the boundary of the metasurface the resonant line becomes less pronounced, a deviation from the ideal continuous line shape, due to the finite array size and the weakening of the quasi-BIC confinement at the boundaries[31].

To further understand the broadening effect of the gradient metasurface, we systematically investigated how the local scaling factor and array size influence the resonance characteristics (Supplementary Note 8). In our design, the scaling factor between adjacent unit cells (S_{near}) is approximately 1.00006, corresponding to an extremely gradual geometric variation. Because the change in geometry between neighboring unit cells is very small, each local region of the metasurface can be regarded as a quasi-periodic array with an almost constant unit-cell geometry. This locally quasi-periodic condition allows the collective high-Q resonance to be preserved, similar to that of a uniform periodic array, while the resonance wavelength is slowly varied across the device. Under this condition, the Q-factor remains effectively unchanged compared to that of a uniform array ($S_{near} = 1$), confirming that high-Q resonances are preserved despite the continuous geometric variation. This preservation of resonance quality enables a key advantage over pixelated metasurface designs, within the same footprint, the gradient metasurface can provide a substantially higher density of spectral data points without sacrificing the Q-factor. Furthermore, we experimentally confirm that high-Q resonances are maintained when the lateral width is reduced to 150 μm (Supplementary Note 9). This allows multiple gradient channels to be integrated within a single device, thereby enabling parallelized operation and further increasing the achievable spectral data density through multiplexing.

In addition, under *y*-polarized illumination, the dark line vanishes from the transmission image, confirming that the observed effect is due to the polarization-selective excitation of quasi-BIC

modes (Supplementary Note 10).

Spectral information was extracted by averaging intensity profiles of the transmission images without using an external spectrometer. To minimize edge effects, the transmitted intensity was averaged over the central region of the metasurface, excluding the edge regions, as a function of horizontal position. To improve data quality, a reference-based normalization was applied by dividing the measured transmission image I by the background image I_0 obtained from the reference substrate without the metasurface. This process effectively suppresses spatial non-uniformity and systematic background variations, reducing baseline fluctuations and oscillatory artifacts. The spatial coordinates were then converted to wavelength using the resonance wavelength spatial map obtained in Fig. 2e (see Supplementary Note 11 for details). This result yields a reconstructed transmission spectrum (Fig. 2h). The normalized spectra in Fig. 2h, obtained from a series of images in Fig. 2g, show a sharp resonance dip. We measured an average full width at half maximum (FWHM) of 2.20 nm, defined as the wavelength difference between the two points at half of the maximum intensity, corresponding to a maximum Q-factor of 398 and an average Q-factor of 345. We note that spatial non-uniformity in the refractive index distribution near the metasurface can slightly distort the resonance lineshape compared to the calibration condition. However, by averaging the intensity over a finite spatial region, these local fluctuations can be mitigated, enabling reliable extraction of the overall resonance shift.

Gradient metasurface characterization

We first evaluated the spectral resolution of our imaging-based gradient metasurface sensor. The illumination wavelength was tuned in fine steps of 0.1 nm, and a transmission image was captured at each step. Even with a moderate 20× objective, the gradient metasurface clearly distinguished a 0.1 nm difference in wavelength, as shown by a detectable shift in the resonance line position between each obtained image (Fig. 3a). Moreover, this fine spectral step size of 0.1 nm is maintained over a ~30 nm spectral window, meaning the device can reliably distinguish very small shifts anywhere within that range (Supplementary Note 12). The spectral step size of the system can be further improved by employing an objective lens with a higher numerical aperture (NA) or an image sensor with higher spatial resolution. However, it should be noted that increasing the NA

reduces the effective spectral coverage, as the field of view decreases, limiting the total spectral coverage across the metasurface. Therefore, a trade-off between spectral resolution and spectral coverage must be carefully considered in system design. In our implementation, the 20× objective was chosen to provide an optimal balance, offering ~0.1 nm spectral step size across ~30 nm of spectral range, which is sufficient for the biosensing demonstrations presented.

Next, we characterized the sensor's sensitivity to uniform refractive index changes in the surrounding medium, i.e., its bulk refractometric sensitivity. Aqueous glycerol solutions of varying concentrations ranging from 0% to 50% were prepared by mixing glycerol (n = 1.473) with deionized water (n = 1.33) to produce controlled refractive index variations. The transmission image of the gradient metasurface was acquired using supercontinuum illumination through a tunable bandpass filter. To ensure a flat optical interface and suppress image distortions or scattering from the liquid surface, a thin cover glass was placed on top of the liquid (Fig. 3b). The resulting transmission image was then converted into a reconstructed spectrum using the resonance wavelength spatial map. Under pure water (0% glycerol), the metasurface exhibited a sharp and well-confined resonance with a high Q-factor. As the glycerol concentration increases, we observed a consistent resonance line shift to the left, reflecting a monotonic red-shift of the resonance (Fig. 3c). Note that this transmission images were obtained under an illumination wavelength of 800 nm, which was used to accommodate higher refractive index samples, as the corresponding resonance shifts extend beyond the spectral window of our gradient metasurface.

To further quantify the refractometric sensing performance, we measured the sensitivity in terms of resonance wavelength shift per refractive index unit (RIU) using certified index-matching oils with known refractive indices of 1.402, 1.458, and 1.550. We performed a wavelength sweep in 0.1 nm increments using the supercontinuum source and identified, through post-processing, the specific wavelengths at which the resonance lines exhibited minimum intensity at the same spatial position across different index-matching oils. This allowed us to directly read off the resonance wavelength for each known refractive index, effectively tracking large spectral shifts. We performed this measurement on three independently fabricated gradient metasurface samples to ensure repeatability, and averaged the results. Our gradient metasurface sensor demonstrated a RIU sensitivity of 147.8 nm/RIU, well matching the simulation result (Supplementary Note 13), with a Q-factor of 345 (FWHM = 2.20 nm), yielding a figure of merit (FOM) defined as RIU

sensitivity divided by FWHM of 67.2 (Fig. 3d). Notably, our gradient metasurface sensor platform simultaneously achieves high sensitivity and FOM, while providing a broad spectral coverage (~30 nm) corresponding to an accessible refractive index range of approximately ± 0.1 RIU, all without the use of a spectrometer, thereby highlighting its suitability for practical sensing applications.

Surface functionalization and biomolecule sensing

To demonstrate the potential of our gradient metasurface sensor as a POC diagnostic platform, we implemented a compact optical setup to fully leverage our imaging-based gradient metasurface sensor. The system consists of a VCSEL laser diode as a monochromatic illumination source with illumination wavelength of 760 nm and a CMOS image sensor for transmission imaging (Fig. 4a). Owing to its significantly narrower spectral linewidth compared to a supercontinuum laser combined with a bandpass filter, the VCSEL laser diode enables a sharper optical response, resulting in higher effective *Q*-factors and improved image contrast (Supplementary Note 14).

Moreover, the small form factors of both the light source and detector allow the entire system to be realized as a highly portable platform (Supplementary Note 15). This imaging-based readout scheme is employed for all sensing experiments described below.

We next demonstrated its utility for specific biosensing by detecting ultrathin molecular layers and low-concentration analytes. The key to specific biosensing is functionalizing the metasurface with a biorecognition layer so that only the target molecule of interest will bind and induce a refractive index change. We employed surface chemistry approaches to immobilize biorecognition molecules on the surface of the metasurface. Two model biosensing scenarios were investigated: (1) a protein-ligand binding assay using biotin and streptavidin, and (2) a nucleic acid hybridization assay using single-stranded DNA probes and target DNA.

To demonstrate the molecule-specific sensing capability of our gradient metasurface sensor, we employed the well-established biotin-streptavidin binding model as a proof-of-concept for detecting ultrathin biomolecular layers. The biotin-streptavidin system is a common model for biosensor evaluation due to its strong affinity and well-understood surface chemistry. We functionalized the metasurface in a stepwise manner to capture streptavidin. First, the surface was

activated with hydroxyl groups (-OH) by piranha cleaning and oxygen plasma treatment. Next, we performed silanization with 3-aminopropyltriethoxysilane (APTES), which forms a self-assembled monolayer of amine-terminated silane on the hydroxylated surface. We then introduced biotin: a solution of sulfo-NHS-biotin was applied, which reacts with the surface amines (APTES layer) to covalently attach biotin molecules, creating a biotin-functionalized surface. Finally, this surface was exposed to the target protein, streptavidin, which binds specifically and tightly to the immobilized biotin sites (Fig. 4b). To verify each functionalization step, we first carried out the chemistry on a uniform metasurface, with constant geometry across the area ($S = 1$), so that it has a single resonance wavelength, and measured the transmission spectrum after each step using a standard spectrometer.

For each functionalization step, we observed a consistent redshift in the resonance wavelength, indicating successful layer-by-layer attachment and a corresponding increase in the local refractive index (Fig. 4c). To further validate molecular immobilization, contact angle measurements were performed at each step of the functionalization process. The resulting contact angle values were consistent with those reported in previous literatures involving biotin-streptavidin surface chemistry, thereby validating the successful immobilization of the molecular layers[32–35] (Supplementary Note 16).

We then applied the same functionalization procedure to the gradient metasurface sensor and utilized our imaging-based readout to monitor the resonance shifts after each step, without an external spectrometer. Consistent redshifts of resonance wavelength were observed in the transmission images following each surface treatment due to the added molecular layers (Fig. 4d). These shifts are in agreement with the spectrometer-based measurements on the uniform sample ($S = 1$), but here they are obtained through simple image analysis. To evaluate the sensitivity of our platform, streptavidin solutions with varying concentrations were applied to the biotin-functionalized surface. Each concentration was applied on an independent metasurface to avoid sequential accumulation. The resulting resonance shifts obtained by reconstructed spectrum from transmission images, exhibited a monotonic increase with streptavidin concentration (Fig. 4e). The resonance shift was fitted using the Langmuir adsorption model, capturing the concentration-dependent surface coverage in affinity-driven interactions. Notably, the limit of detection (LOD) was estimated based on the IUPAC (International Union of Pure and Applied Chemistry) definition,

where the minimum detectable signal is defined as the mean blank signal plus three times its standard deviation ($\mu + 3\sigma$). The corresponding LOD in concentration was then determined by identifying the intersection between this threshold signal level and the fitted Langmuir adsorption curve, with the *x*-coordinate of the intersection taken as the LOD. The resulting LOD of 388.5 pM is comparable to previously reported high-sensitivity platforms[24,36]. Furthermore, to evaluate performance under more biologically relevant conditions, we conducted the streptavidin-biotin binding assay in a buffer environment. In this case, an LOD of 3.44 nM was achieved, with an average *Q*-factor of 342 and a FWHM of 2.22 nm (Supplementary Note 17).

However, unlike many spectrometer-based approaches, our method requires only a simple imaging setup based on a VCSEL diode and a CMOS image sensor, making it suitable for portable sensing applications with a potentially more cost-effective readout architecture.

To demonstrate the versatility and specificity of our gradient metasurface sensor, we extended its application to nucleic acid detection. By enabling the sensitive and specific identification of specific DNA or RNA sequences, nucleic acid sensing is central to many diagnostic tests such as cancer, infectious diseases, and genetic disorders. It also supports personalized medicine by guiding treatment decisions and monitoring therapeutic responses, often through minimally invasive methods such as liquid biopsy. However, because single-stranded DNA has a inherently low refractive index and forms ultra-thin layer, label-free optical detection of DNA hybridization is challenging compared to other biomolecules such as proteins[37].

We implemented a two-step “click chemistry” functionalization to covalently attach ssDNA probes onto the metasurface. First, the surface was treated with piranha cleaning and oxygen plasma treatment. We silanized the surface with 3-azidopropyltriethoxysilane (AzPTES), which creates a monolayer presenting azide ($-N_3$) groups. Next, we introduced a 20-base-long ssDNA sequence probe DNA functionalized with a dibenzocyclooctyne (DBCO) group at its 5′ end. The DBCO reacts with the azide on the surface via strain-promoted alkyne-azide cycloaddition (SPAAC), a copper-free click chemistry reaction, forming a stable covalent bond that binds the DNA probe to the surface (Fig. 5a). This strategy yields a densely grafted layer of ssDNA probes on the metasurface.

We verified the DNA functionalization by fluorescence microscopy using Cy3-labeled version of

the DBCO-ssDNA strands. After ssDNA incubation, intense and uniform fluorescence signal was observed across silanized regions, indicating efficient and spatially homogeneous DNA attachment. In contrast, the azide-functionalized regions without DBCO-DNA treatment exhibited negligible fluorescence, whereas strong fluorescence was observed in regions modified with fluorescence labeled DBCO-DNA, confirming the uniform azide-DBCO conjugation (Supplementary Note 18). Surface wettability changes during functionalization steps were also monitored by contact angle measurements. The initial contact angle of the bare a-Si:H surface exhibited ~90°, which decreased to 75° following AzPTES treatment and further to 23° after DNA immobilization, which aligns well with the inherently hydrophilic nature of DNA strands (Supplementary Note 18).

For the biosensing test, the probe-functionalized metasurface was exposed to target DNA solutions. We chose a specific 20-mer DNA sequence, complementary to the probe, as the target and also prepared a non-complementary 20-mer mismatch DNA, to test specificity. After introducing the target DNA sample and rinsing, we captured the transmission image using our VCSEL laser diode-based portable setup and extracted the reconstructed spectrum. Figure 5b shows the reconstructed spectrum before and after treating with 100 μM target DNA, as well as after treating with 100 μM mismatch DNA. The resonance undergoes a clear red-shift upon hybridization with complementary DNA, whereas the mismatch DNA produces only a negligible shift. We then measured a range of concentrations for both target and mismatch DNA. As shown in Fig. 5c, the resonance shift extracted from the reconstructed spectrum of the transmission images increases with target DNA concentration, showing a resonance shift of 0.08 nm at 100 pM and 0.56 nm at 100 μM. The response follows a sigmoidal binding curve, which is fitted using the Hill equation.

In contrast, mismatch DNA at equivalent concentrations produces significantly smaller resonance shifts, remaining below the estimated LOD of 3.93 nM, thereby enabling clear discrimination between specific and non-specific binding. While this LOD is higher than that for the biotin-streptavidin model, due to the weaker binding affinity and smaller refractive index change of the DNA, it is still notable for a label-free optical method without amplification. In addition, the minor shifts observed for mismatch DNA are attributed to residual nonspecific physical adsorption. These results highlight the potential of our imaging-based gradient metasurface sensor for nucleic acid testing, which is a key component of modern medical diagnostics.

Discussion

We have demonstrated a spectrometer-free, imaging-based metasurface biosensor that combines high sensitivity and fine spectral resolution with a broad spectral window in a compact spatial footprint. By introducing a continuous geometry gradient in a dielectric metasurface, we effectively encode different resonance wavelengths across the device, enabling quasi-continuous spectral readout via a single camera image. Our platform achieved an average Q-factor 345 and an FOM 67.2, and we demonstrated label-free detection of both proteins and DNA at clinically relevant concentrations using this platform. The key advantages of our approach include the ability to detect minute spectral shifts without any spectrometer, the high spectral resolution afforded by the high-Q quasi-BIC resonance, and the wide spectral coverage (~30 nm) enabled by the gradient design. This unique combination addresses the trade-offs faced by previous nanophotonic sensors, offering both the precision of high-Q resonances and the flexibility of broad spectral window within a single system.

Compared to previous imaging-based sensors that use high-Q, pixelated resonators[4,20,21,29], our gradient metasurface provides direct spectral readout from a single transmission image with higher Q-factor, FOM, and spectral coverage (Supplementary Note 19). Moreover, in pixelated designs, spectral resolution is fundamentally limited by the number and spacing of discrete resonant pixels. Such architectures are intrinsically constrained by a trade-off between pixel size and resonance Q-factor. Consequently, maintaining high-Q resonances requires sufficiently large pixel sizes, which fundamentally limits the achievable spectral resolution per unit area.

In our gradient design, every point along the metasurface is effectively a different resonator, creating a continuum of resonance positions. This creates a nearly continuous spectral response across the entire range, enabling a substantially higher density of resolvable spectral channels and finer spectral resolution without significant change in the Q-factor, with the ultimate resolution mainly determined by the imaging system. In essence, the gradient metasurface functions analogously to a compact spectrometer, where the wavelength is directly determined from the position of the resonance-induced feature, effectively converting spatial position into spectral information. Unlike previous gradient metasurfaces[38], particularly SEIRA-based

implementations[39], which rely on bulky broadband mid-infrared optical systems and reconstruct absorption spectra through sequential acquisition and stitching of spatially scanned images, our approach operates under single-wavelength illumination using a monochromatic VCSEL diode laser. In contrast of measuring broadband absorption, our platform performs refractometric sensing by tracking resonance shifts induced by refractive index changes. These shifts are directly translated into spatial intensity shifts, enabling the sensing signal to be retrieved from a single-shot image. As a result, our method eliminates the need for broadband sources and spectroscopic instrumentation, enabling a compact, low-cost, and portable sensing platform.

The demonstrated label-free and specific detection of streptavidin and DNA highlights the practical biosensing capabilities of the platform. Moreover, the imaging-based readout also opens up possibilities for multiplexed detection: in principle, multiple different regions of the metasurface could be functionalized with different receptors (e.g., DNA probes or antibodies) to detect multiple analytes simultaneously, all read out by one camera, as long as their resonance shifts remain within the device's spectral range.

Further refinement of the metasurface design holds promise for enhancing both performance and scalability. The overall *Q*-factor is primarily limited by fabrication imperfections, which introduce variations in unit-cell geometry and reduce the coherence of the collective resonance. Separately, in its current form, quasi-BIC mode formation is weaker near the device edges, which limits the fully active sensing area and consequently constrains miniaturization and multiplexing. By enabling strong resonance confinement in smaller, more localized regions, future designs could reduce the overall device size and fabrication cost without compromising sensitivity. Additionally, while our current fabrication process relies on electron-beam lithography for high-resolution nanopatterning and precise structural fidelity, future implementation of scalable nanofabrication techniques could improve high-throughput. In particular, nanoimprint lithography[18,19,40], offers a promising pathway, as it can replicate nanostructures with high fidelity over large areas once a high-quality master mold is fabricated. Deep ultraviolet (DUV) lithography may also provide a viable and industrially scalable approach with sufficient resolution and uniformity[26]. This advancement in fabrication techniques would pave the way for compact, disposable optical biosensors for real-world POC diagnostics.

Importantly, compared with conventional high-Q optical refractometric sensing systems that typically require broadband illumination sources and high-resolution spectrometers to track resonance wavelength shifts, our platform offers a potentially more cost-effective sensing architecture by replacing these components with a compact VCSEL diode and a CMOS image sensor. This simplified optical readout configuration enables the system to be miniaturized into a portable platform while maintaining a high Q-factor and sensing performance. This transition significantly enhances the translational potential of the technology, bridging the gap between laboratory-scale demonstrations and practical POC diagnostics.

In summary, the imaging-based gradient metasurface sensor exemplifies how nanophotonic engineering can push the boundaries of biosensor performance while also addressing practical constraints. By integrating high-Q photonic resonances with spatial encoding and a compact VCSEL-based optical system, we developed a sensor platform that is highly sensitive, specific, and scalable, without the need for complex instrumentation. These results pave the way for ultrasensitive POC diagnostics, bringing advanced molecular testing out of specialized labs and into routine clinical and field use.

Methods

Numerical simulation

Numerical simulations were conducted using the commercially available finite element method (FEM) solver COMSOL Multiphysics 6.1, and a commercially available Lumerical FDTD 2024 R1. The simulations of the transmission spectrum, electric, and magnetic field were performed using periodic boundary conditions in the *x*-and *y*-directions and perfect boundary conditions in the *z*-direction.

Device fabrication

Hydrogenated amorphous silicon (a-Si) was deposited on a glass substrate using plasma-enhanced chemical vapor deposition (HiDep-SC, BMR Technology) at 200 °C and 30 mTorr. The deposition time was 82 s, resulting in an approximately 100-nm-thick a-Si film. The refractive index and thickness of the deposited film were measured using a spectroscopic ellipsometer (M-2000, J.A. Woollam). For patterning, a positive-tone electron-beam resist, ZEP-520A (Zeon), diluted in anisole at a 1:1 ratio, was spin-coated onto the a-Si film at 3000 rpm for 60 s, followed by soft baking at 180 °C for 4 min, yielding an approximately 130-nm-thick resist film. Electron-beam lithography was then performed using an ELS-7800 system (Elionix) with an exposure time of 0.45 μs/dot and a beam current of 100 pA. The exposed resist was developed in ZED-N60 at 0 °C for 4 min 20 s to form a hole-patterned ZEP etch mask. The pattern was transferred into the a-Si layer by dry etching using a silicon/metal hybrid etcher (DMS) with SF_6 and CHF_3 gases at a flow-rate ratio of 20:60 for 17 s, generating periodic holes through the 100-nm-thick a-Si film. After etching, the remaining ZEP mask was removed in anisole at 45 °C for 1 h. The fabricated metasurface was then observed using scanning electron microscopy (Hitachi Regulus8100), confirming the formation of the desired hole-patterned a-Si structure.

Streptavidin surface functionalization

The surface functionalization protocol was designed to create a uniform biotin-terminated surface on metasurfaces for high-affinity streptavidin binding. The protocol employed sequential

silanization with 3-aminopropyltriethoxysilane (APTES, Sigma Aldrich) followed by biotin conjugation via sulfo-NHS-biotin chemistry.

Metasurface substrates were sequentially cleaned in acetone, isopropanol, and deionized water (1 min each) to remove organic contaminants. Following solvent cleaning, metasurfaces were treated with oxygen plasma (100 W, 10 min) to generate surface hydroxyl groups essential for subsequent silanization. A 10% (v/v) APTES solution was prepared in anhydrous ethanol immediately before use. Cleaned metasurfaces were immersed in the APTES solution for 2 hours at room temperature, then rinsed with ethanol and blow-dried with nitrogen gas. Thermal curing at 130°C for 30 minutes was performed to complete the condensation reaction, yielding a uniform aminosilane monolayer. Sulfo-NHS-biotin (MW 443.43 g/mol) (Thermo Fisher) was dissolved in PBS (pH 7.4) immediately before use. A 20 μL droplet was deposited on each sample and incubated in a humid chamber at room temperature for 2 hours. The reaction forms stable amide bonds between primary amines and NHS ester groups, resulting in covalently attached biotin moieties. After biotinylation, metasurfaces were rinsed with PBS and subjected to 5-minute ultrasonication in PBS to remove unreacted reagents and non-specifically adsorbed materials. Metasurfaces were then blow-dried with nitrogen gas. A 1 mg/mL streptavidin (Sigma Aldrich) stock solution was prepared in PBS and serially diluted to create concentrations ranging from 16.7 μM to 0.167 nM (10^{-1} to 10^{-6} dilutions). Each sample received 20 μL of streptavidin solution and was incubated in a humid chamber at room temperature for 2 hours to achieve binding equilibrium. Final metasurface processing included PBS rinsing followed by PBS immersion with 5-minute ultrasonication to remove unbound streptavidin while preserving specifically bound molecules. Metasurfaces were nitrogen-dried and stored until optical characterization. In parallel, unfunctionalized metasurfaces on the same substrate were maintained as reference samples at each functionalization step. These reference regions were used to monitor potential environmental or instrumental drift by confirming that no significant resonance shift occurred in the absence of surface modification, thereby ensuring that the observed spectral changes originate from specific biomolecular binding.

Each step of the surface functionalization was verified by measuring the static contact angle using a goniometer (SmartDrop, FemtoBiomed Inc.). Deionized water was used as the probing liquid for the contact angle measurements.

DNA surface functionalization

The surface functionalization protocol was developed to covalently immobilize DNA strands onto metasurface substrates *via* strain-promoted azide-alkyne cycloaddition (SPAAC) chemistry. The procedure employed silanization using 3-azidopropyltriethoxysilane (AzPTES, Gelest), followed by conjugation with dibenzocyclooctyne (DBCO)-functionalized DNA.

Metasurface substrates were sequentially cleaned in acetone and isopropanol (1 min each) to remove organic contaminants. Following solvent cleaning, the substrates were treated with oxygen plasma (70 W, 15 min) to generate surface hydroxyl groups essential for subsequent silanization. A 0.2 mM AzPTES solution was prepared in anhydrous toluene, with 0.1% (v/v) trifluoroacetic acid (TFA) added as a silanization catalyst. Cleaned metasurfaces were immersed in the silane solution and incubated for 18 hours at room temperature. Following silanization, samples were rinsed with fresh toluene, blow-dried with nitrogen gas, and annealed in a 70°C oven for 1 hour to complete the condensation process.

For DNA attachment, a 100 μM solution of DBCO-functionalized single-stranded DNA (5′-DBCO-Cy3-T_{12}-CTCTCACC-3′, Integrated DNA Technologies, USA) was prepared in PBS (pH 7.4) and loaded onto the silanized surfaces. Samples were incubated at 55°C for 24 hours to allow covalent conjugation between azide and DBCO moieties. After incubation, unreacted DNA strands were removed by rinsing with PBS, followed by 5 minutes of sonication in PBS to eliminate nonspecifically adsorbed molecules. The substrates were washed with deionized water and dried under a nitrogen stream.

Optical measurement

The optical characterization employed a transmission-mode configuration with supercontinuum laser (SuperK FLANIUM, NKT Photonics), tunable bandpass filters (LLTF Contrast, NKT Photonics), linear polarizer, 20× objective lens, and monochrome CCD camera (INFINITY3, Lumenera). The wavelength map of the metasurface was obtained by scanning the illumination wavelength from 745 to 775 nm in 0.1 nm increments, with an exposure time of 100–1000 ms per

wavelength point. For each wavelength, the pixel with the minimum intensity was identified and used to construct the corresponding wavelength map.

The portable optical setup is composed of 760 nm wavelength VCSEL laser diode (L760VH1, Thorlab), linear polarizer, 20× objective lens, and CMOS sensor (G3M178M).

Data Availability

The data that support the plots within this paper and other finding of this study are available within the article, its supplementary information, or from the corresponding author upon reasonable request.

References

1. Altug, H., Oh, S.-H., Maier, S. A. & Homola, J. Advances and applications of nanophotonic biosensors. *Nat. Nanotechnol.* **17**, 5–16 (2022).
2. V. Kabashin, A., G. Kravets, V. & N. Grigorenko, A. Label-free optical biosensing: going beyond the limits. *Chem. Soc. Rev.* **52**, 6554–6585 (2023).
3. Neubrech, F., Huck, C., Weber, K., Pucci, A. & Giessen, H. Surface-Enhanced Infrared Spectroscopy Using Resonant Nanoantennas. *Chem. Rev.* **117**, 5110–5145 (2017).
4. Im, H. *et al.* Label-free detection and molecular profiling of exosomes with a nano-plasmonic sensor. *Nat. Biotechnol.* **32**, 490–495 (2014).
5. Tseng, M. L., Jahani, Y., Leitis, A. & Altug, H. Dielectric Metasurfaces Enabling Advanced Optical Biosensors. *ACS Photonics* **8**, 47–60 (2021).
6. Minopoli, A. *et al.* Ultrasensitive antibody-aptamer plasmonic biosensor for malaria biomarker detection in whole blood. *Nat. Commun.* **11**, 6134 (2020).
7. Shrivastav, A. M., Cvelbar, U. & Abdulhalim, I. A comprehensive review on plasmonic-based biosensors used in viral diagnostics. *Commun. Biol.* **4**, 70 (2021).
8. Chen, J. I. L., Chen, Y. & Ginger, D. S. Plasmonic Nanoparticle Dimers for Optical Sensing of DNA in Complex Media. *J. Am. Chem. Soc.* **132**, 9600–9601 (2010).
9. Kim, I. *et al.* Metasurfaces-Driven Hyperspectral Imaging via Multiplexed Plasmonic Resonance Energy Transfer. *Adv. Mater.* **35**, 2300229 (2023).
10. Ren, Z., Zhang, Z., Wei, J., Dong, B. & Lee, C. Wavelength-multiplexed hook nanoantennas for machine learning enabled mid-infrared spectroscopy. *Nat. Commun.* **13**, 3859 (2022).
11. Rodrigo, D. *et al.* Mid-infrared plasmonic biosensing with graphene. *Science* **349**, 165–168 (2015).
12. Li, Y. *et al.* Graphene Plasmon Enhanced Vibrational Sensing of Surface-Adsorbed Layers. *Nano Lett.* **14**, 1573–1577 (2014).
13. Lee, I.-H., Yoo, D., Avouris, P., Low, T. & Oh, S.-H. Graphene acoustic plasmon resonator for ultrasensitive infrared spectroscopy. *Nat. Nanotechnol.* **14**, 313–319 (2019).
14. Zhou, H. *et al.* Surface plasmons-phonons for mid-infrared hyperspectral imaging. *Sci. Adv.* **10**, eado3179 (2024).
15. Kuznetsov, A. I., Miroshnichenko, A. E., Brongersma, M. L., Kivshar, Y. S. & Luk'yanchuk, B. Optically resonant dielectric nanostructures. *Science* **354**, aag2472 (2016).
16. Caldarola, M. *et al.* Non-plasmonic nanoantennas for surface enhanced spectroscopies with ultra-low heat conversion. *Nat. Commun.* **6**, 7915 (2015).
17. Rybin, M. V. *et al.* High-Q Supercavity Modes in Subwavelength Dielectric Resonators. *Phys. Rev. Lett.* **119**, 243901 (2017).
18. Choi, M. *et al.* Roll-to-plate printable RGB achromatic metalens for wide-field-of-view holographic near-eye displays. *Nat. Mater.* **24**, 535–543 (2025).
19. Kim, J. *et al.* Scalable manufacturing of high-index atomic layer–polymer hybrid

metasurfaces for metaphotonics in the visible. *Nat. Mater.* **22**, 474–481 (2023).
20. Tittl, A. *et al.* Imaging-based molecular barcoding with pixelated dielectric metasurfaces. *Science* **360**, 1105–1109 (2018).
21. Yesilkoy, F. *et al.* Ultrasensitive hyperspectral imaging and biodetection enabled by dielectric metasurfaces. *Nat. Photon.* **13**, 390–396 (2019).
22. Koshelev, K., Lepeshov, S., Liu, M., Bogdanov, A. & Kivshar, Y. Asymmetric Metasurfaces with High-Q Resonances Governed by Bound States in the Continuum. *Phys. Rev. Lett.* **121**, 193903 (2018).
23. Koshelev, K., Favraud, G., Bogdanov, A., Kivshar, Y. & Fratalocchi, A. Nonradiating photonics with resonant dielectric nanostructures. *Nanophotonics* **8**, 725–745 (2019).
24. Wang, J. *et al.* All-Dielectric Crescent Metasurface Sensor Driven by Bound States in the Continuum. *Adv. Funct. Mater.* **31**, 2104652 (2021).
25. Kim, H. *et al.* Optical Metasurfaces for Biomedical Imaging and Sensing. *ACS Nano* **19**, 3085–3114 (2025).
26. Leitis, A., Tseng, M. L., John-Herpin, A., Kivshar, Y. S. & Altug, H. Wafer-Scale Functional Metasurfaces for Mid-Infrared Photonics and Biosensing. *Adv. Mater.* **33**, 2102232 (2021).
27. Leitis, A. *et al.* Angle-multiplexed all-dielectric metasurfaces for broadband molecular fingerprint retrieval. *Sci. Adv.* **5**, eaaw2871 (2019).
28. Kühner, L. *et al.* Radial bound states in the continuum for polarization-invariant nanophotonics. *Nat. Commun.* **13**, 4992 (2022).
29. Jahani, Y. *et al.* Imaging-based spectrometer-less optofluidic biosensors based on dielectric metasurfaces for detecting extracellular vesicles. *Nat. Commun.* **12**, 3246 (2021).
30. Hong, T., Li, D. & Valentine, J. G. Metasurface-enabled barcoding for compact flow cytometry. *Optica* **11**, 577–582 (2024).
31. Liu, Z. *et al.* High-Q Quasibound States in the Continuum for Nonlinear Metasurfaces. *Phys. Rev. Lett.* **123**, 253901 (2019).
32. Gunda, N. S. K., Singh, M., Norman, L., Kaur, K. & Mitra, S. K. Optimization and characterization of biomolecule immobilization on silicon substrates using (3-aminopropyl)triethoxysilane (APTES) and glutaraldehyde linker. *Appl. Surf. Sci.* **305**, 522–530 (2014).
33. Williams, E. H. *et al.* Immobilization of streptavidin on 4H–SiC for biosensor development. *Appl. Surf. Sci.* **258**, 6056–6063 (2012).
34. van Oss, C. J. *et al.* Macroscopic-scale surface properties of streptavidin and their influence on aspecific interactions between streptavidin and dissolved biopolymers. *Colloids Surf. B Biointerfaces* **30**, 25–36 (2003).
35. Gajos, K. *et al.* Spatially selective biomolecules immobilization on silicon nitride waveguides through contact printing onto plasma treated photolithographic micropattern: Step-by-step analysis with TOF-SIMS chemical imaging. *Appl. Surf. Sci.* **506**, 145002 (2020).
36. Bontempi, N. *et al.* Highly sensitive biosensors based on all-dielectric nanoresonators.

Nanoscale **9**, 4972-4980 (2017).

37. Inagaki, T., Hamm, R. N., Arakawa, E. T. & Painter, L. R. Optical and dielectric properties of DNA in the extreme ultraviolet. *J. Chem. Phys.* **61**, 4246–4250 (1974).
38. Sinev, I. *et al.* Chirality encoding in resonant metasurfaces governed by lattice symmetries. *Nat. Commun.* **16**, 6091 (2025).
39. Richter, F. U. *et al.* Gradient High-Q Dielectric Metasurfaces for Broadband Sensing and Control of Vibrational Light-Matter Coupling. *Adv. Mater.* **36**, 2314279 (2024).
40. Kim, J. *et al.* A water-soluble label for food products prevents packaging waste and counterfeiting. *Nat. Food* **5**, 293–300 (2024).

Funding

This work was financially supported by the POSCO-POSTECH-RIST Convergence Research Center program funded by POSCO, and National Research Foundation (NRF) grants (RS-2024-00462912) funded by the Ministry of Science and ICT (MSIT) of the Korean government. This reseach was supported by a grant of Korean ARPA-H Project through the Korea Health Industry Development Institute (KHIDI), funded by the Ministry of Health & Welfare, Republic of Korea (Grant number: RS-2025-25454431). H.K. acknowledges the Asan Foundation Biomedical Science fellowship, and the Presidential Science fellowship funded by the MSIT of the Korean government. H.Y. acknowledges the Presidential Science fellowship funded by the MSIT of the Korean government, the NRF Quantum Science fellowship (RS-2024-00402302) funded by the MSIT of the Korean government, and the NRF M.S. fellowship (RS-2024-00358185) funded by the Ministry of Education (MOE).

Author contributions

J.R. conceived the ideas and initiated the project. H.K. developed the concepts and designed the whole experiments. H.K. designed the metasurfaces. H.K., S.J. and H.Y. conducted optical biorecognition experiments. H.Y., S.J., Y.Y. and E.L. fabricated the metasurface sensors. S.J., H.K., H.Y., M.R., and H.L. conducted surface chemistry. H.K., H.Y. and S.J. prepared the manuscript. J.J, C.J., M.J. and Y.-S.R. were partially involved in writing the manuscript. All the authors participated in discussions and confirmed the final manuscript. J.R. guided the entire work.

Competing interests

The authors declare no competing interests.

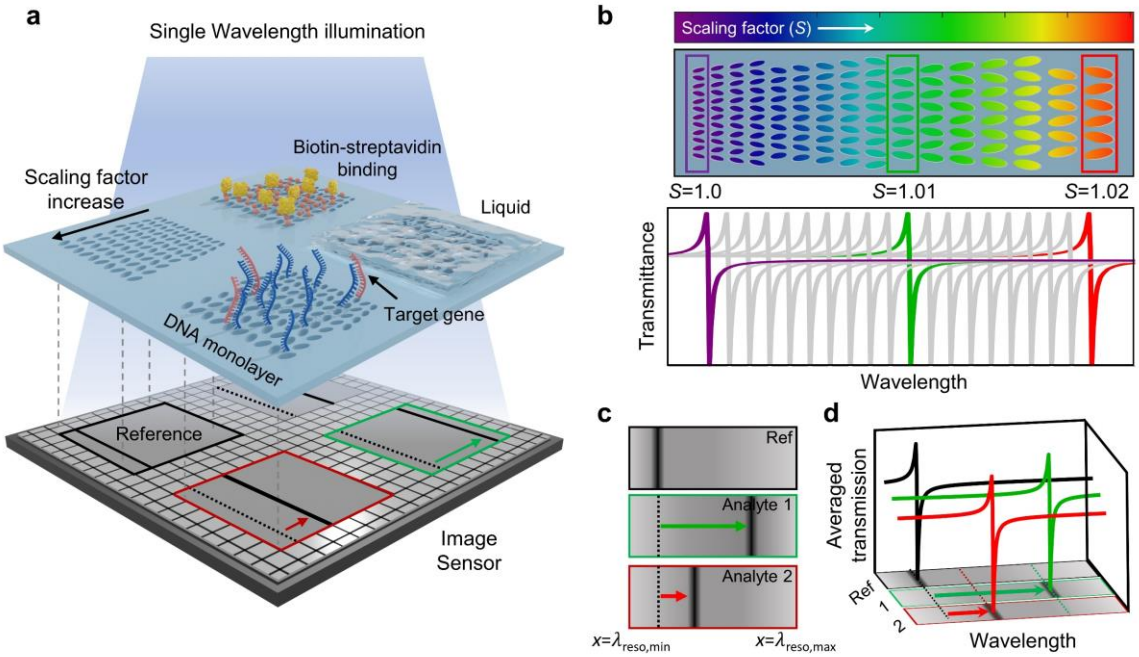

Fig. 1. Imaging-based gradient metasurface biosensing platform. a, Schematic of the imaging-based biosensing setup using gradient metasurface under single-wavelength illumination. **b,** The metasurface encodes distinct resonance wavelengths across its surface by gradually varying the unit cell geometry along the horizontal axis, assigning each spatial position a distinct transmission spectrum. **c,** Illustration of a transmission image showing sharp resonant dark line at the resonant position, which shifts laterally upon target biomolecule binding. **d,** Reconstructed spectrum from the spatial intensity profile in **c**, demonstrating a high-*Q* resonance.

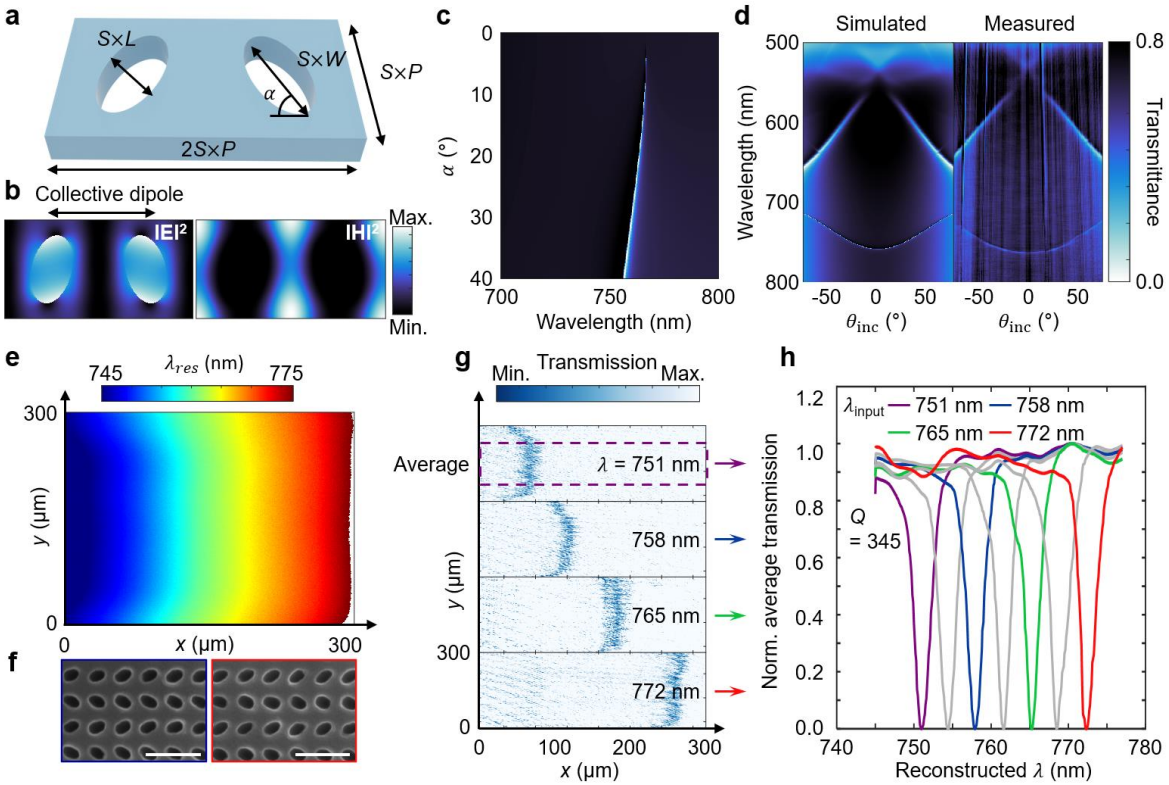

Fig. 2. Gradient metasurface supporting quasi-BIC resonance. a, Schematic of the designed unit cell. **b,** Simulated electric and magnetic field of metasurface with $S = 1$ at $\lambda = 760$ nm. **c,** Simulated transmission spectra of the metasurface with varying tilt angle (α). **d,** Simulated and measured transmission band dispersion with geometry of $P = 340$ nm, $W = 240$ nm, $L = 144$ nm, and $S = 1.02$. **e,** Measured resonance wavelength spatial map of the fabricated metasurface **f,** SEM images taken from each horizontal side of metasurface (blue, red rectangle). Scale bar: 500 nm. **g,** Transmission image of the metasurface where x-polarized single wavelength is illuminated with varying wavelength. **h,** Normalized transmission spectra for each illumination wavelength obtained from **g**, where half of the image was taken and averaged for each horizontal position. S: Scaling factor; W: long-axis of the elliptical hole; L: short-axis of the elliptical hole; P: Period.

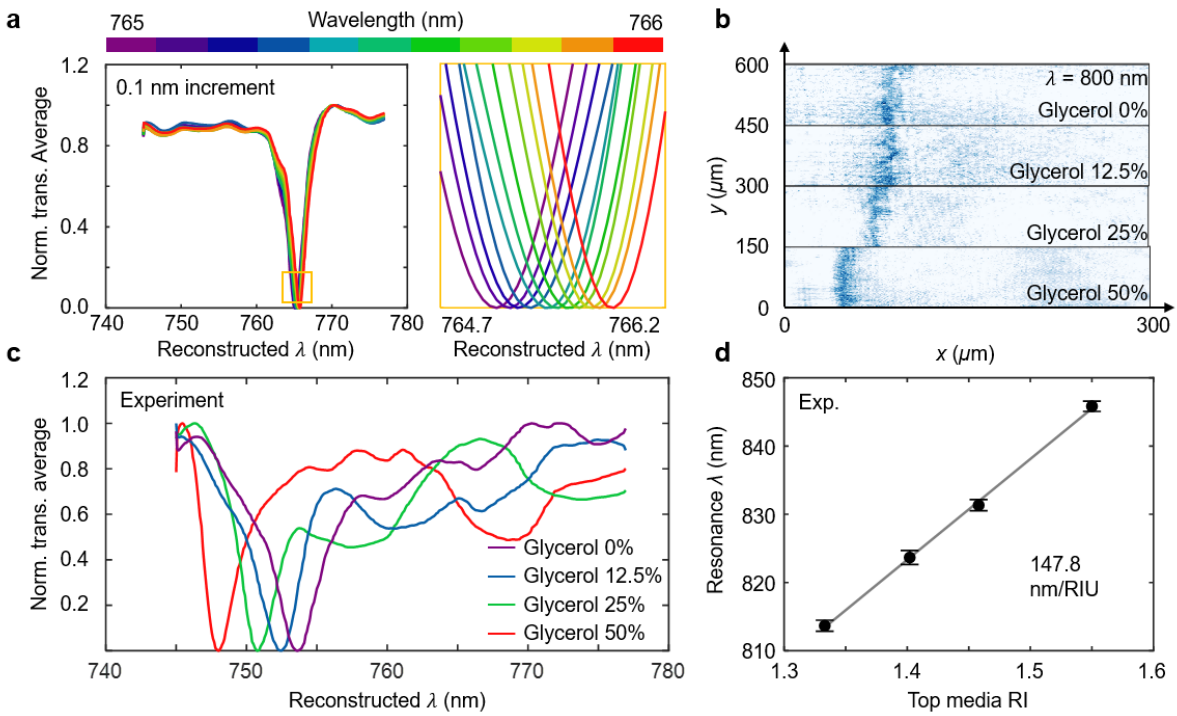

Fig. 3. Spectral resolution and sensitivity of gradient metasurface sensor. a, Measured spectral data of the metasurface as the illumination wavelength is varied from 765 nm to 766 nm with 0.1 nm increments. Inset shows a magnified view of the spectral response, resolving fine spectral shifts. **b,** Transmission image of the metasurface illuminated at $\lambda = 800$ nm, with a glycerol-water mixture layered on top. **c,** Normalized reconstructed transmission spectra for each glycerol concentration obtained from **b**, where half of the image was taken and averaged for each horizontal position. **d,** Measured resonance wavelength shift of the metasurface in response to oils with varying refractive indices. Data points represent the mean values from three independently fabricated gradient metasurface samples, and error bars represent the corresponding standard deviations.

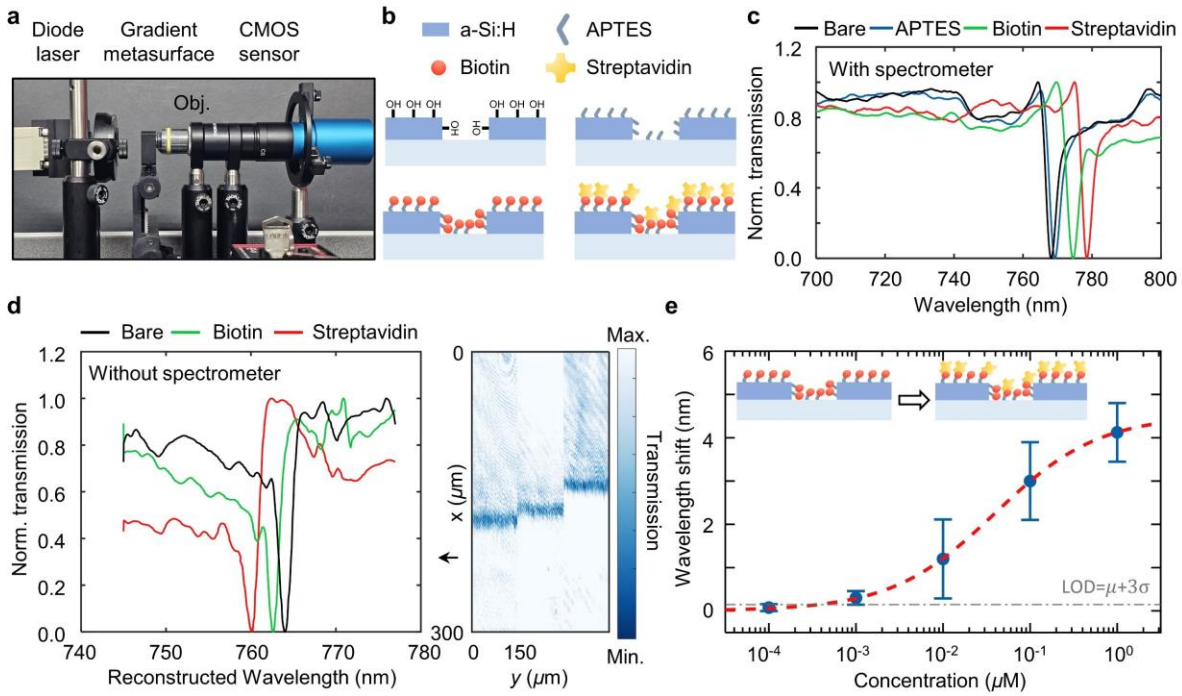

Fig. 4. Biosensing demonstration using the biotin-streptavidin binding model. a, Portable optical sensing setup composed of VCSEL laser diode, gradient metasurface and a CMOS sensor. **b,** Schematic illustration of the surface functionalization steps for streptavidin-specific sensing. **c,** Transmission spectra measured by a spectrometer after each surface functionalization step for metasurface with constant scaling factor ($S = 1$) over entire spatial area. **d,** Transmission responses measured for each functionalization setup using the imaging-based gradient metasurface sensor with the portable VCSEL laser diode-based setup (λ = 760 nm). **e,** Resonance wavelength shifts corresponding to varying streptavidin concentrations, demonstrating the detection capability of the imaging-based gradient metasurface sensor. Data points represent the mean values from 12 independent measurements performed using metasurfaces located on different substrates, and error bars represent the corresponding standard deviations.

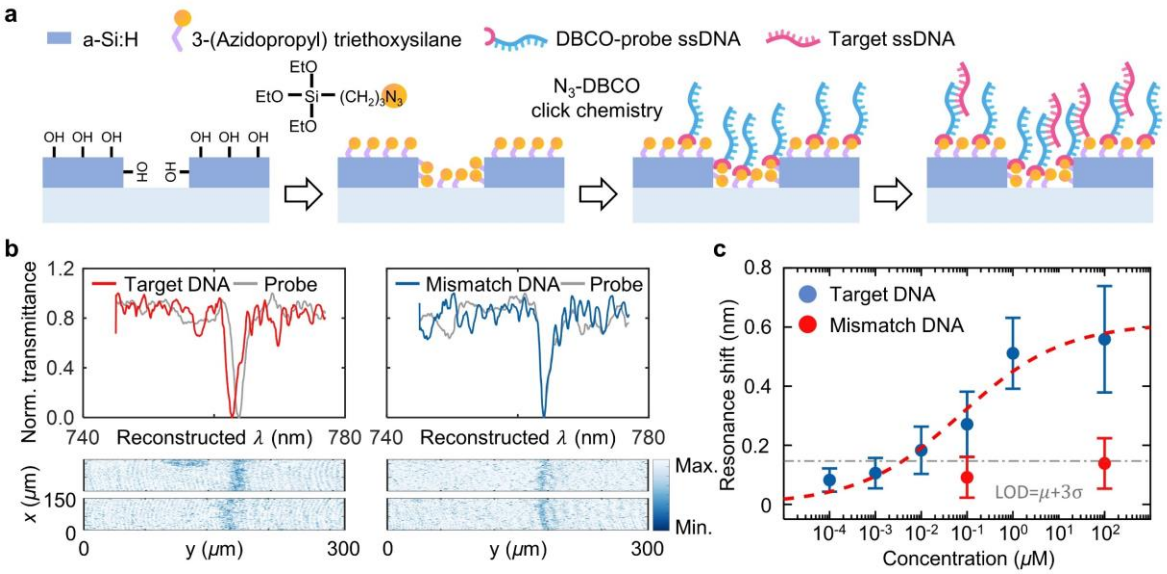

Figure 5. Demonstration of nucleic acid sensing using the gradient metasurface sensor. a, Schematic illustration of the surface functionalization steps for target DNA sequence sensing. **b,** Measured reconstructed spectra extracted from transmission image for target DNA treatment and mismatch DNA treatment compared to probe DNA step, using the VCSEL laser diode-based portable setup (λ = 760 nm). **c,** Resonance wavelength shifts as a function of target DNA and mismatch DNA concentrations. The dashed line represents a fitted line to the Hill equation, and the data points represent the mean values from 12 independent measurements performed using metasurfaces located on different substrates, and error bars represent the corresponding standard deviations.